- View **PDF**
- Download full issue
  Search ScienceDirect

## Outline

## Cited by (2)

## Figures (7)



Graphic Abstract: Heterostructures formed by phase transition of Ag₂FeSnS₄
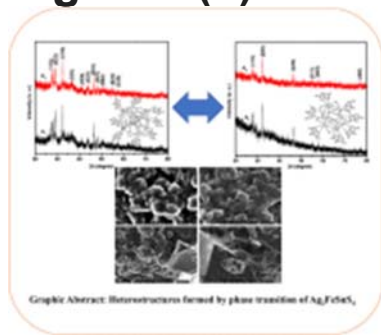
1.
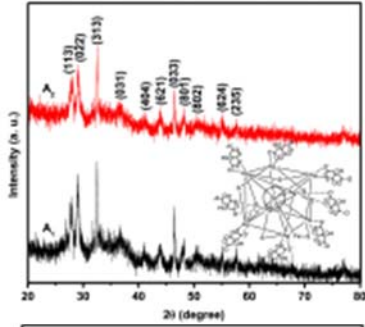
2.



3.
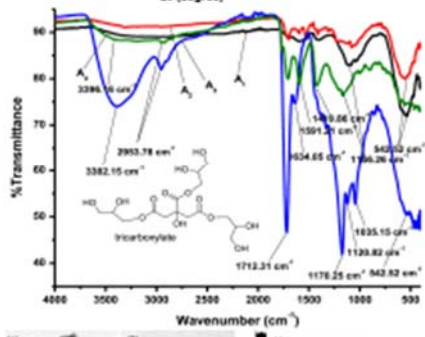


4.
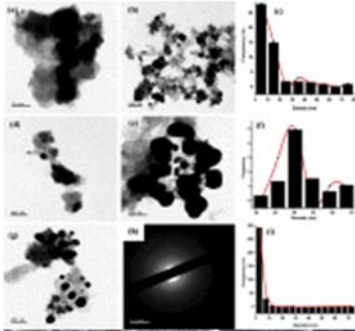


5.
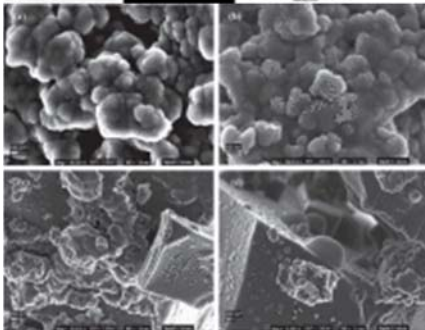


6.



Show 1 more figure

# Extras (1)

1. Document

# Heterostructures of Ag₂FeSnS₄ chalcogenide nanoparticles as potential photocatalysts

Author links open overlay panelJoseph Adeyemi Adekoya [a], Michael Onyedikachi Chibuokem [a], Siphamandla Masikane [b], Neerish Revaprasadu [b]
Show more
Add to Mendeley
Share
Cite

## Abstract

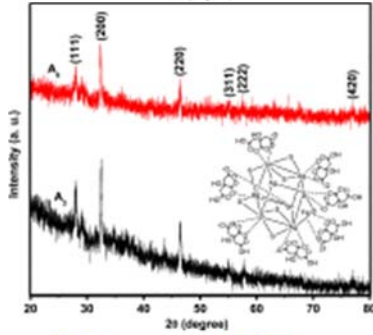The synthesis of photocatalysts with a suitable bandgap that could speed up the rate of oxidation of chemical effluent is of utmost importance to material chemists. It has been observed that chalcogenide nanostructures research continues to dominate scientific work over the last few years based on their exciting bandgap within the semiconductor bandgap range. In this research work, novel class $I_2$-II-IV-VI$_4$ quaternary chalcogenides nanoparticles were synthesised using co-precipitation by varying the reaction conditions of temperature (200 °C and 250 °C) and, essentially, capping agents (citric acid and glycerol) and the mole ratio of precursors. The resulting nanoparticles were purified and vacuum dried to give a black crystalline solid. The Powder-X-ray Diffraction analysis of the as-synthesised heterostructure chalcogenides showed novel pure phase materials

that exhibited the orthorhombic and cubic $Ag_2FeSnS_4$ crystal systems reminiscent of the parent compounds $Ag_8SnS_6$ and $AgSnS_2$ under different experimented reaction conditions. The morphological characterisation of the HC chalcogenides by Transmission Electron Microscope revealed that the nanomaterials formed were predominantly nanocubes, with particle diameters ranging from 22.98 ± 1.67 to 57.26 ± 12.93 nm. Further elucidation of the optical property of the HC nanoparticles by Tauc's plot based on the data derived from UV-Vis spectrophotometry measurement revealed that the bandgap ranged from 1.58 to 1.99 eV. The FTIR absorption character of the as-synthesised HC nanoparticles provided evidence for the surface functionalisation, confirming the presence of moieties like the hydroxyl (O-H) at 3396.16 cm$^{-1}$ and carbonyl group (C=O) at 1712.31 cm$^{-1}$. At the same time, the UV-Visible spectrophotometry, measured over a range of 250 to 1000 nm, showed broad absorbance between 420 and 800 nm, confirming the optical property of the nanoparticles. The result showed that heterostructure chalcogenide nanoparticles would have an excellent photocatalytic application.

# Graphical abstract



Graphic Abstract: Heterostructures formed by phase transition of Ag₃FeSnS₄
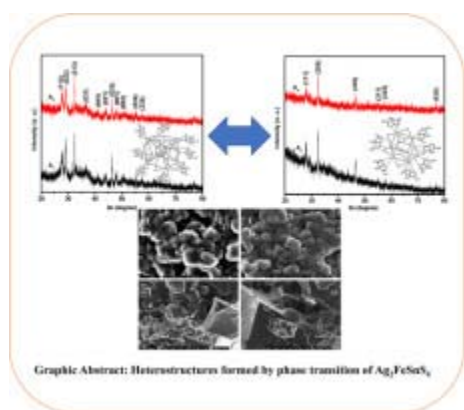
1. Download: Download high-res image (157KB)
2. Download: Download full-size image
   .

# Keywords

Chalcogenide
Nanoparticles
Photocatalyst
Heterostructure
Co-precipitation

# Introduction

Water pollution is one of the world's most significant issues today. The implementation of several purification methods to curb the issue of water pollution is fast becoming a topical research focus. Photo and electrocatalysis are the recent mechanisms utilised to purify water [1,2]. As one of the very significant resources to man and the environment, "a drop of water is more valuable than gold to a thirsty man" is a famous saying that explains the importance of clean and pure water over materials luxury [3]. Water pollution and scarcity of safe drinking water are two of the world's most serious environmental problems, having severe repercussions for natural ecosystems and living beings. With the growing demand for human material life, people are paying more attention to water ecosystems than ever before, resulting in the development of various water treatment methods. The fast advancement of agriculture and global industry, which has resulted in many forms of pollution, is one of the factors necessitating the development of viable wastewater treatment [4]. Organic wastes have been released due to growing industrialisation and human activities, posing a threat to the environment and human health. Therefore, experts attempt to discover alternative techniques for reducing or eliminating these pollutants.

Filtration, flocculation, and adsorption are physical waste treatment procedures that can separate unwanted colloidal components from water. Still, wastewater decontamination by chemical reactions is critical [5,6]. Many researchers have always been interested in treating organic dyes in micro-polluted water. Traditional procedures for removing such stains are incompatible with current water resources and water quality requirements. The use of active semiconductor photocatalysts to treat environmental pollutants in wastewater has recently gotten a lot of interest because of its capacity to decompose organic toxins into carbon dioxide, hydrogen, and mineral acids [7,8]. It is in line with Goal 7 of Africa's Union's Agenda 2063, which focuses on environmentally sustainable and climate-resilient economies and communities. It enshrines sustainable natural resource management and biodiversity conservation, sustainable consumption and production patterns with water security. From a global perspective, this research addresses Sustainable Development Goal 6 which involves water sanitation and hygiene and also addresses the quality and sustainability of water resources, which are critical to the survival of people and the planet.

Practical approaches involving the use of binary semiconductors, such as $TiO_2$, CdS [9], ZnO [10], $Fe_2O_3$ [11], and $C_3N_4$ [12], have been considered to degrade a wide range of organic pollutants, converting them into less toxic forms in which they are mineralised into carbon (IV) oxides and water. As potent as these arrays of semiconductors are, they are ladened with a few limitations ranging from poor photostability, band structure, and high recombination rates at the fermi levels. Therefore other approaches to address these limitations involved using ternary oxides or a combination of binary oxides and chalcogenides to produce a direct or indirect z-scheme photo-oxidation process that would produce holes and electrons at the excited states. These holes and electrons, thus initiated through the photovoltaic effect, usually facilitate the photooxidation of organic pollutants. Moreover, there are a few limitations to the photocatalysis potential of binary chalcogenides when used alone as semiconductors because they suffer from self-oxidation, leading to photo corrosion.

As a rider, the use of multijunction semiconductors has been investigated to mitigate this effect of self-oxidation arising from the application of a combination of binary metal

oxides to wastewater treatment. Some of these include $Bi_2WO_6$/BiOCl p-n heterojunction which was prepared by hydrothermal synthesis using precursor solution containing sodium tungstate, bismuth nitrate pentahydrate and hydrochloric acid. The resulting morphologies of the as-prepared nanoparticles were microspheres and nanosheets [13]. A type II p-n heterostructures of $Co_3O_4$/$BiVO_4$ were prepared by Zhao et al. [14] using a similar approach at a reaction temperature of 180 °C for 10 h. The electrodeposition method was used by Cao et al. [15] to prepare $Ag_3PO_4$/$BiVO_4$ for wastewater treatment. A 100% removal of 5 $mgL^{-1}$ norfloxacin was achieved after 90 min. In recent times, multijunction systems such as metal oxides/chalcogenides ZnO/$TiO_2$/$Ag_2Se$ semiconductor of the N-n-n type prepared by electrodeposition from the requisite precursors facilitated 96.5% decay of oxytetracycline in an urban wastewater treatment study [16]. All of these put together make it possible to consider a wide array of materials designed with a potential energy gap in the range of photocatalysts that could be used in wastewater remediation.

Therefore, a new approach in which ternary and binary semiconductor chalcogenides are designed and combined through morphology-controlled synthesis to provide nanomaterials with potential optical properties for the photo or electrocatalytic oxidation of organic pollutants to less harmful or toxic intermediates is being considered. The ingenuity of this method lies in the choice of eco-friendly capping reagents and the relatively cheap and abundant mineral precursors to synthesise either a phase pure or composite quaternary heterostructure chalcogenides with potential optical properties for the management of organic wastes. Secondly, these materials may also be possible alternative water-splitting photocatalysts sources.

Herein, we report a novel facile method for synthesising heterostructure chalcogenide semiconductors comprising group I-II-IV-VI elements. The morphology-controlled synthesis of heterostructure semiconductors was achieved by optimising the temperature of the reaction, using citric acid alone or with glycerol in a co-precipitation gravimetric approach under nitrogen gas purge, and varying the mole ratio of precursor inorganic salts containing the requisite chemical elements.

# Materials and methods

## Materials

All chemicals, *i.e.,* methanol, acetone, iron(II) sulphate, tin(II) nitrate, silver nitrate, sulphur, citric acid (CA), and glycerol (GLY), were purchased from Sigma Aldrich and used without further purification.

## Synthesis of $Ag_xFeSnS_y$ nanoparticles

Silver Source: Silver Nitrate ($AgNO_3$), Tin source: Tin nitrate $Sn(NO_3)_2$, Iron source: Iron chloride ($FeCl_2$). In a typical procedure, 0.05 moles of sulfur powder was dissolved in 20 mL of deionised water in a three-necked flask. 0.1 moles of $NaBH_4$ dissolved in 20 mL deionised water was added to this mixture and left to stir for 12 h under a nitrogen atmosphere at room temperature. 0.033 moles of silver nitrate salt ($AgNO_3$),

alongside 0.0167 moles of tin nitrate $Sn(NO_3)_2$ were added to the reduced sulfur and left to stir at room temperature for 30 min. The bulk FeS was also synthesised by reacting the reduced sulphur with iron chloride salt ($FeCl_2$) in an aqueous solution, following the same procedure for forming the ternary materials under continuous nitrogen purge. The solution also was left to stir at room temperature for 30 min. Both the $Ag_xSnS_y$ and the FeS bulk thus synthesised were washed using a mixture of methanol and acetone. The mixed chalcogenide nanoparticles were formed by adding an equimolar amount of both ternary $Ag_xSnS_y$ and binary FeS bulk materials to citric acid or glycerol and heating the mixture to 200 °C or 250 °C while stirring under continuous nitrogen purge. Purification of the as-prepared STFS colloidal dispersion was carried out by copiously washing it with a mixture of methanol and acetone, followed by centrifuging and drying in a vacuum desiccator to obtain the dry nanoparticles. Table S1 shows the various conditions in synthesising the heterostructure chalcogenide nanoparticles (HC NPs). The following equations of reaction (1) – (4) show the various stages in forming the heterostructure chalcogenides nanoparticles, while Fig. S1 represents the crystal lattice of the as-synthesised Ag-based heterostructure chalcogenide nanoparticles.

$$(1)\ 4NaBH_4(aq)+2S(s)+7H_2O(l) \xrightarrow{Reflux/250C/12h/N_2} 2NaHS(aq)+Na_2B_4O_7(aq)+14H_2$$

$$(2)\ xAg^+(aq)+Sn^{2+}(aq)+yS^{2-}(aq) \xrightarrow{Reflux/250C/30min/N_2} Ag_xSnS_y(aq)$$

$$(3)\ S^{2-}(aq)+Fe^{2+}(aq) \xrightarrow{Reflux/250C/30min/N_2} FeS(aq)$$

$$(4)\ Ag_xSnS_y(aq)+FeS(aq)+CA(aq) \xrightarrow{Reflux/2000C/30min/N_2} Ag_xFeSnS_y-CA(aq)$$

The resulting quaternary nanoparticles have the structures and geometry of orthorhombic and cubic systems with the unit cell organisation and coordination centre depicted in Fig. S1. In the orthorhombic system, each Sn atom is coordinated to eight Ag atoms in a manner that the indexed atoms occupy the vertices of a regular rhombohedron (Fig. S1a, b). In contrast, the cubic system comprises the Ag and Sn atoms alternating at the cube's vertices (Fig. S1c). The crystal structure of SFTS was deduced from the analysis of acquired powder X-ray diffraction data.

## Characterisation

The following characterisation techniques were used to analyse the synthesised heterostructure chalcogenide nanoparticles: Fourier Transform Infrared spectra of the dry NPs were recorded in the range 400–4000 cm$^{-1}$. A solution of the NPs in ethanol was sonicated at 50°C and analysed with a PerkinElmer Lambda 1050 UV-Vis NIR spectrometer to carry out optical absorbance measurement of the HC NPs in the wavelength range 250–1000 nm. Powder XRD diffraction studies of the vacuum-dried HC NPs were performed on a Bruker AXS D8 diffractometer using Cu-Ka radiation ($\lambda$ = 1.54178 Å) at 40 kV, 40 mA, room temperature. The samples were mounted flat and scanned between 20 and 90° in a step size of 0.05 with a count of 10 s. The ethanolic solution of the HC NPs, after sonication was analysed with a JEOL 1010 TEM to characterise the samples' morphology and particle sizes with an accelerating voltage of 100 kV, Megaview III camera, and Soft Imaging Systems TEM software. The dry HC NPs was gold-coated by sputtering and a Zeiss Ultra Plus FEG Scanning Electron Microscope (SEM), equipped with an Oxford detector EDX at 20 kV and Aztec software afforded the surface morphology and elemental analysis of the nanoparticles.

# Results and discussion

## Powder X-ray Diffraction patterns of heterostructure chalcogenide nanoparticles

The p-XRD pattern of dry powder HC NPs obtained at 200 °C by the heat-up method in a citric acid solution of a 1:1 mole Ag-Sn: Fe precursor is shown in **Fig.** 1A$_1$. At the same time, a summary of the crystallographic and morphological properties of this heterostructure and other analogues prepared under varying conditions of reaction is presented in Table S2. Upon phase analysis with the Match! X-ray powder diffraction software, the crystallographic character of the heterostructure represents a predominantly pure orthorhombic phase of Ag$_8$SnS$_6$ (ICDD# 96-150-9987) parent material with a space group of (*Pna*2(1)) for the 200°C reactions using 1:1 mole of Ag-Sn and Fe precursors. The reflections at 2θ = 27.81°, 29.12°, 32.56° and 46.47° corresponding to the (113), (022), (313) and (033) planes of orthorhombic (Ag$_8$SnS$_6$) are the higher intensity peaks, but the (022) indicates a directional orientation or significant growth of the crystal along (022) plane. There is no evidence of multiple sets of peaks for binary Ag$_2$S, SnS or FeS phases, which shows the formation of single-phase crystalline Ag$_x$FeSnS$_y$ NPs. Moreover, the crystallite size was estimated by using the Scherrer formula:
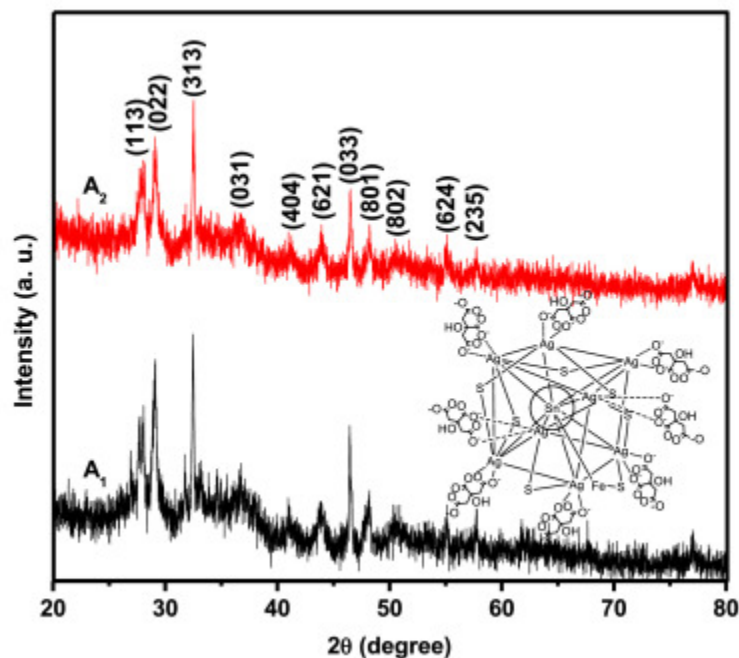


1. Download: Download high-res image (382KB)
2. Download: Download full-size image
   Fig. 1. p-XRD pattern of Ag$_2$FeSnS$_4$ NPs (matched with orthorhombic Ag$_8$SnS$_6$ parent compound) at 200 °C with a 1:1 mole of Ag-Sn: Fe precursors (A$_1$); 1.3:1 mole of Ag-Sn: Fe precursors (A$_2$) when CA was used as coordinating solvent and surfactant (heat up). $\tau = K\lambda\beta Cos\theta$ where $\tau$ is the mean size of the ordered crystalline domains, K is the dimensionless shape factor close to unity, $\lambda$ is the x-ray wavelength, $\beta$ is the line broadening at half the maximum intensity and $\theta$ is the Bragg's angle. The crystallite size

based on the (113) and (022) planes is ca. 45.54 nm for citric acid-derived HC NPs at 200 °C.

Using a similar approach, Du et al. also obtained the orthorhombic phase of $AgInS_2$ and $CuInS_2$ by an improved solvothermal process using hexadecyl amine as a capping agent. The colloidal monodispersed pyramidal nanoparticles were 13-17 nm in size [17]. However, Delgado et al. successfully synthesised a new *P*-chalcopyrite compound $Cu_2FeIn_2Se_5$ that exhibited the parent's chalcopyrite structure $CuInSe_2$ in the p-XRD pattern [18]. Their work and several others confirmed the possibility of a quaternary material, like ours retaining the crystal structure of its parent ternary phase [19,20]. Moreover, the difference in dislocation density and microstrain of the crystal lattice of SFTS NPs prepared with a different mole of Ag-Sn: Fe precursor $2.83 \times 10^{-3}$ $nm^{-2}$ and $0.32 \times 10^{-3}$, respectively, in Table S2, is due to expansion in the core ionic radius interstices of the cavity formed by the orthorhombic system.

The Rietveld refinement of $Ag_xFeSnS_y$ nanoparticles obtained at 200 °C with 1:1 mole of Ag-Sn: Fe precursors in citric acid using FullProf Suite in conjunction with Match! offered a complete convergence and reduced chi-square as shown in Fig. S2. All the major peaks indicated acceptable average Bragg R-factor, confirming the identification of the experimental diffraction pattern by phase matching.

A similar characteristic phase of the orthorhombic crystal system also was found by others using different synthetic procedures, ranging from sulfurisation of Ag-Sn salt precursor [21] to simple chemical synthesis [22], electrodeposition technique [23], solution growth and solventless synthesis [24]. Hu et al. [24] were able to predict a submicron pyramid model with four outer surfaces $(\overline{4}11)$, $(112)$, $(21\overline{1})$ and $(4\overline{1}3)$ which are integral part of the orthorhombic system. However, in the case of our model structure, the four planes based on the orthorhombic geometry are predicted to be (113), (022), (313) and (033) (Fig. 1), because they present the more fitting symmetry and lattice spacing identical to diffraction pattern of the experimental materials under study.

The crystallographic data for subsequent semiconductor SFTS NPs synthesised at 200 °C using a different mole ratio of 1.3:1 Ag-Sn: Fe (Fig. $1A_2$) presents a similar pure phase orthorhombic structure. There is no evidence of mackinawite (FeS), pyrite ($FeS_2$), or other analogues in the powder crystallographic pattern of the synthesised SFTS nanoparticles. The variation in the mole ratio of the precursors has no significant impact on the crystalline phase of the heterostructure chalcogenide. Table S2 summarises the crystallographic properties of SFTS HC prepared with a mole 1.3:1 Ag-Sn: Fe at 200 °C. There is no significant difference in the lattice parameters. The space group remains $Pna21$, while the lattice constant ($d_{022}$ spacing), dislocation density, microstrain, and $I_{022}/I_{313}$ peak intensity differ marginally.

The crystallite size of 1.3:1 mediated SFTS nanoparticles (17.39 nm) estimated by the Scherrer equation at (113) and (022) planes is relatively smaller than that of the 1:1 Ag-Sn: Fe precursor (45.54 nm), showing the possibility of distortion of the orthorhombic symmetry and reinforcing the nanostructuring ability of the coordinating solvent at a moderate temperature under varying mole ratios of precursors.

Furthermore, varying the reaction condition by employing a mixture of coordinating solvents (citric acid and glycerol) to facilitate the reduction and nucleation of the precursors Ag-Sn and Fe at 200°C gave a different diffraction pattern (Fig. $2A_3$). The

powder diffraction was matched to the parent cubic crystal of $AgSnS_2$ (ICDD# 96-150-9523) with a space group of Fm-3m and lattice parameter a = 5.54197 Å. Notably, replacing the mixed solvent medium with only citric acid and heating the reaction to 250 °C gave rise to a diffraction pattern (Fig. 2A$_4$) depicting a phase transition and a crystal system of the exact symmetry as SFTS in CA/GLY at 200 °C. In this instance, temperature, one of the critical factors responsible for thermodynamic equilibrium reaction, precipitated the occurrence of a different crystal phase where Ag and Sn occupy alternate positions at the vertices of a regular cube. The CA/GLY passivated SFTS crystallite size estimated by the Scherrer equation at 200 °C is 61.53 nm, while the one formed by decomposition in CA at 250 °C was no different than 71.07 nm. In both cases, the indexed reflection planes at (111) and (200) that gave the full width at half maximum (FWHM) exhibited a peak broadening effect. Meanwhile, no evidence of binary FeS, $Ag_2S$ or SnS phases appeared in the powder diffraction pattern of SFTS NPs, either in CA/GLY at 200 °C or in CA at 250 °C.
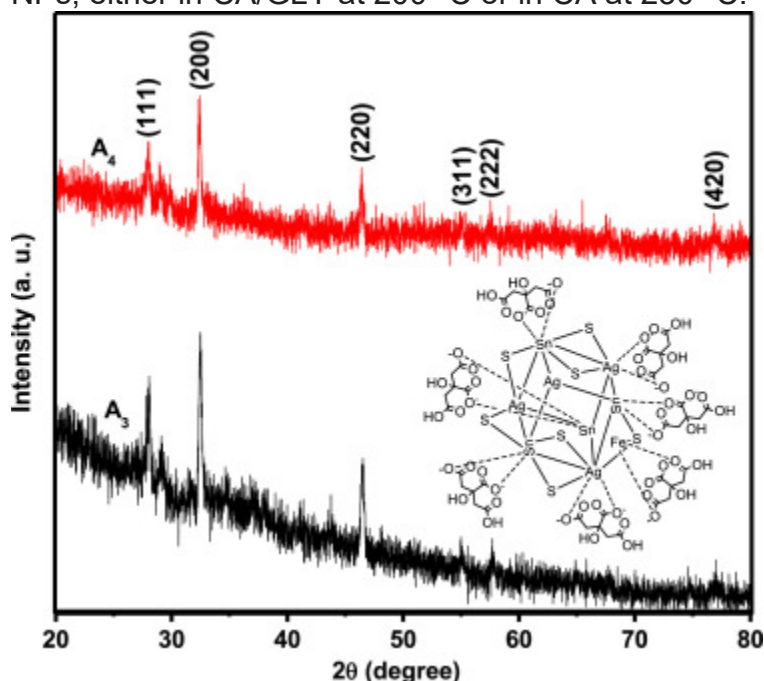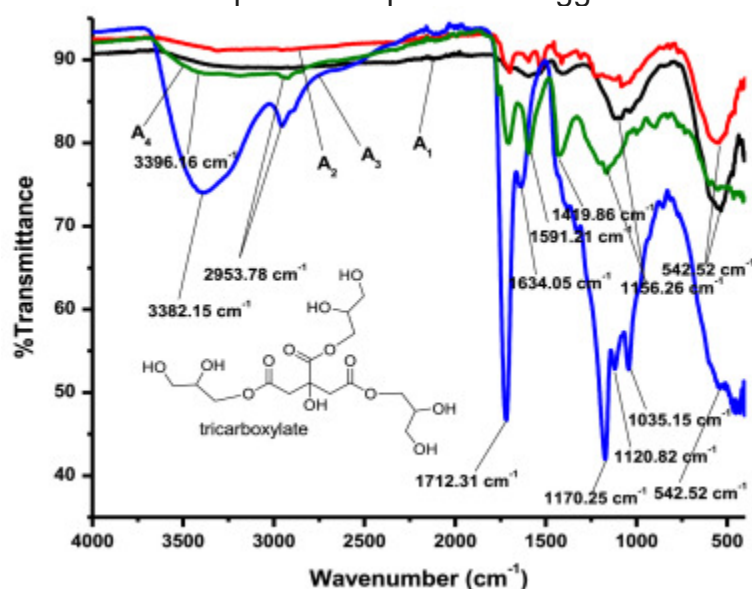


1. Download: Download high-res image (377KB)
2. Download: Download full-size image

Fig. 2. p-XRD pattern of cubic $Ag_2FeSnS_4$ NPs (matched with cubic $AgSnS_2$ parent compound) with 1:1 mole of Ag-Sn: Fe precursors at 200 °C (A$_3$) when CA/GLY were used as coordinating solvent and surfactant and at 250 °C (A$_4$) when CA was used as coordinating solvent and surfactant (heat up).

The structural identification of the powder X-ray diffraction pattern acquired for $Ag_xFeSnS_y$ nanoparticles obtained at 200 °C with a 1:1 mole of Ag-Sn: Fe precursors in citric acid/glycerol was clarified further with a Rietveld refinement. A complete convergence occurred with an average Bragg R-factor greater than 80 and a reduced chi-square of 1.6, as shown in Fig. S3.

## Fourier transform infrared spectrometry analysis of $Ag_xFeSnS_y$ NPs

The IR absorption bands of the quaternary chalcogenides Ag$_x$FeSnS$_y$ NPs are presented in (Fig. 3). Also, the assignment of the absorption bands to the functional groups in Table S3 shows evidence of the surface capping of the Ag$_x$FeSnS$_y$ system by citric acid or a combination of citric acid and glycerol. The long chain alkylated organic acid helped to stabilise the ternary chalcogenide during the Oswald ripening process that involves nucleation and particle growth. The surface-active organic acid acted in the solution phase by passivating the interface with the hydroxyl -OH group, making it functional to aid particle dispersion or agglomeration.



1. Download: Download high-res image (352KB)
2. Download: Download full-size image

Fig. 3. FTIR spectra of Ag$_x$FeSnS$_y$ NPs in CA at 200 °C, 1:1 mole ratio (A$_1$); 1.3:1 mole ratio (A$_2$); CA/GLY at 200 °C, 1:1 mole ratio (A$_3$) and CA at 250 °C, 1:1 mole ratio (A$_4$). The absorption bands for the SFTS NPs at 200 °C (A$_1$ and A$_2$) and 250 °C (A$_4$) are very similar, indicating that the capping moieties are thermally stable at both temperatures. The characteristic absorptions of SAS NPs are due to the stretching vibrations of 3396 cm$^{-1}$ (O-H stretch; acid), 1706 cm$^{-1}$ (C=O stretch; carbonyl of acid), 1591-1420 cm$^{-1}$ (C-H bend; methylene), 1156 cm$^{-1}$ (C-O-C stretch; acyl), and 542 cm$^{-1}$ (M-S fingerprint); confirming the presence of organic acid capping group at the interface. Similar reports were presented by Selvakannan et al. [25]. They prepared gold nanoparticles using wet chemical reduction in the presence of amino acid lysine, which renders the gold nanoparticles water dispersible. Hence, the role of capping agents more often is to control the surface activity and solubility of as-prepared nanoparticles, taking advantage of the hydrophilicity or hydrophobicity of the capping moiety and the active nanoparticles. In essence, the morphology of the colloidal nanoparticles also determines the extent of the surface functionalisation.

It is noteworthy that ternary chalcogenide nanoparticles arising from two or more precursors are easily hydrolysable in polar organic compounds [26,27].

Moreover, the capping activity of a mixture of citric acid and dodecanethiol produced a different pattern of IR absorption in Fig. 3(A$_3$). The major absorption bands of CA/GLY capped SFTS NPs at 200 °C are due to the stretching frequencies, v of 3382 cm$^{-1}$ (O-H

stretch), 2954 cm$^{-1}$ (C-H aliphatic, sp$^3$ C-H stretch), 1712 cm$^{-1}$ (ester C=O stretch), 1591 cm$^{-1}$ (C=C), 1420 cm$^{-1}$ (C-O-C str), and 543 cm$^{-1}$ (M-S fingerprint) due to a tricarboxylate formed by the condensation of the carboxylic acid and hydroxyl groups of a polyol. Once again, the activity of the organic compound formed by these surfactants determined the surface functionality of SFTS NPs.

## Morphological properties of heterostructure chalcogenide nanoparticles

The morphological properties of the identified orthorhombic nanoparticles prepared in citric acid at 200 °C as observed under a Transmission electron microscope are shown in Fig. 4. At the same time, a summary of their particle size is presented in Table S2.
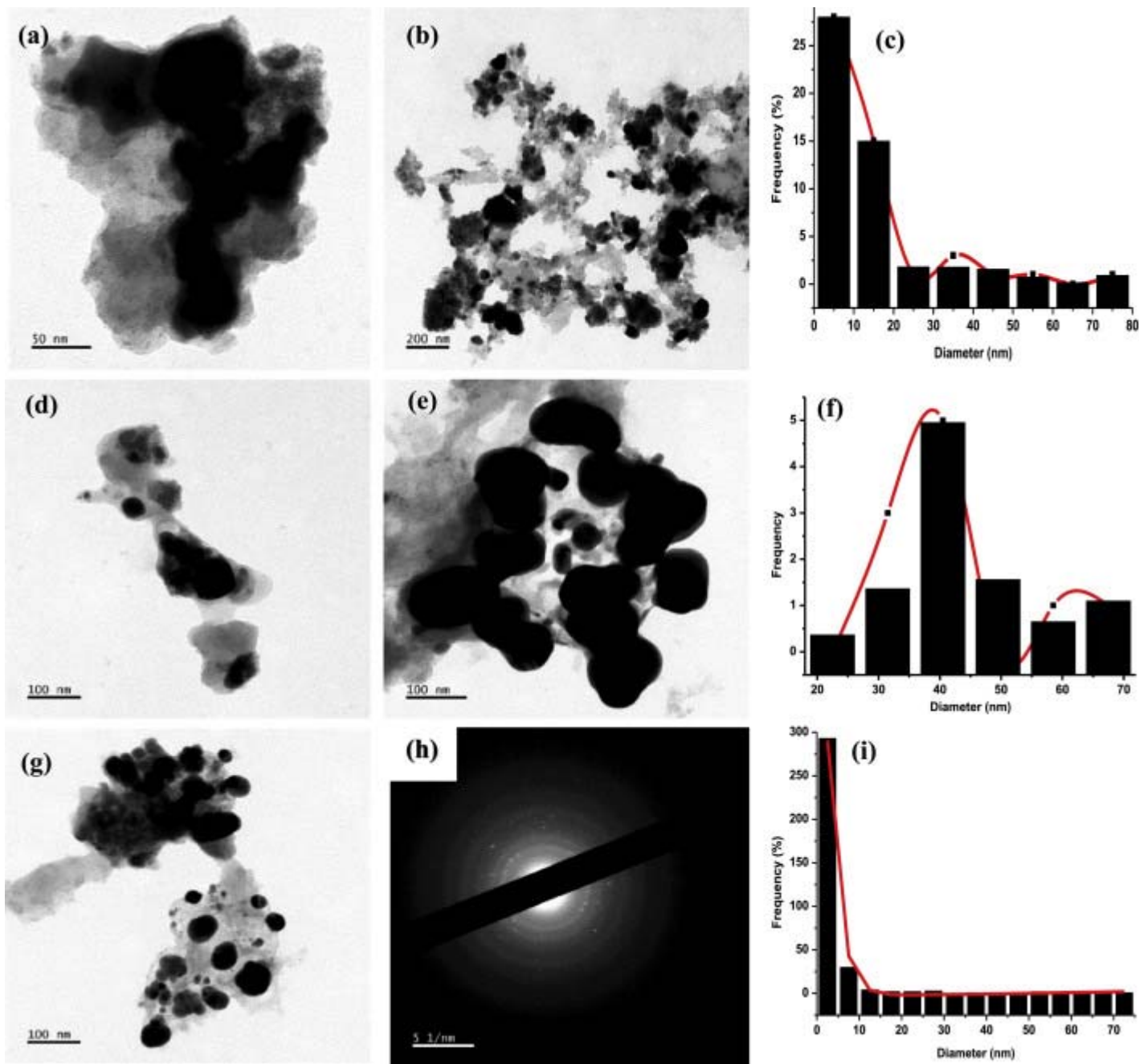
Fig. 4. TEM micrographs of (a) SFTS nanocubes in CA; (b) CA/GLY obtained by heat up at 200 °C with 1:1 mole of Ag-Sn: Fe precursors; (c) particle size histogram of (a); (d) SFTS nanocubes in CA obtained by heat up at 200 °C with 1.3:1 mole of Ag-Sn: Fe precursors; (e, g) SFTS pseudo-nanocubes obtained by heat up in CA at 250 °C with 1:1 mole of Ag-Sn: Fe precursors (h) their selected area electron diffraction (SAED) and (f, i) particle size histograms of (b, e), respectively.

The TEM images show evidence of nanocubes to corroborate the identified phase of the XRD pattern. $Ag_2FeSnS_4$ gave an average particle diameter ranging from 21.31 to 70.19 nm. The size regime is evidence of the nanostructuring effect of a capping agent

with hydrolysing functional group. In CA, the quaternary chalcogenides exhibited the most significant quantum size effect with a particle diameter of 40.76 ± 5.31 (Fig. 4d) when a 1.3:1 mole of Ag-Sn: Fe was used as precursors. Moreover, CA/GLY solvated precursor at 200 °C gave monodispersed $Ag_2FeSnS_4$ NPs (Fig. 4b) with a particle size of 64.11 ± 3.18 nm. The particle size histogram (Fig. 4f) reflects the monodispersity of the SFTS nanoparticle and presents an estimated frequency of 8 – 10 particles measuring up to 40 nm in diameter.

The role played by a mixture of citric acid and glycerol coordinating solvents cannot be overemphasised, as it contributed to an increase in the product yield and subsequently capping of the nanoparticles to enhance their monodispersity. A rider to our work on the capping efficiency of these multifunctional group coordinating solvents can be seen in Al-Salim et al. [28], who selectively prepared hexagonal or cubic phase of $CdSe_xS_y$ nanocrystals in trioctylphosphine oxide, trioctylphosphine, triphenylphosphine, oleylamine, hexadecyl amine, dioctylamine, trioctylamine, and 1-octadecene.

Further confirmation of the role of mixed surfactants in enhancing the capping efficiency of ternary or quaternary chalcogenides is referenced in the works of Khan et al. [29], Adekoya et al. [30], and Hoisang et al. [31]. They demonstrated the synergistic effects of a mixed coordinating solvent on capping efficiency with a combination of oleylamine and dodecanethiol, ethylene diamine and oleic acid, and hexane and oleylamine. In each case, the phase or morphological properties of the as-synthesised chalcogenides were significantly affected and, in turn, the optoelectronic character of the ternary or quaternary semiconductor.

Moreover, the inclusion of CA alone, as seen in the TEM images of the quaternary chalcogenides, resulted in agglomeration at 200 °C (Fig. 4a) and 250 °C (Fig. 4e). It suffices to state that the bulky nature of the organic acid and its hydrophobic alkyl chain might contribute to this effect. Furthermore, it can be ascribed to an increase in columbic or hydrophilic interaction after ethanol sonication which bundled the HC NPs [32], [33], [34]. A similar observation was made by Kush and Deka [35] and Manyar et al. [36]. They observed that alternative routes excluding the use of surfactant to cap or passivate precursor in the synthesis of binary or multinary semiconductors reduced the occurrence of agglomeration.

The selected area electron diffraction (SAED) of SFTS nanoparticles (Fig. 4h) confirmed the presence of crystalline nanoparticles. Each concentric ring in the SAED represents indexed reflection planes discussed in the diffraction pattern. The crystallinity degree is estimated at 14.27%, while the amorphous content is 85.73%. It suggests an agreement between the X-ray diffraction data and the electron micrograph data, which further alludes to the existence of pure-phase quaternary SFTS chalcogenide nanoparticles.

The SEM images of the silver iron tin sulphide synthesised at 200 and 250 °C in citric acid and citric acid/glycerol, and at different mole ratios of precursors are shown in Fig. 5. Citric acid capped SFTS nanoparticles (Fig. 5a) clearly show agglomerated cluster-like nanocubes that are fairly monodispersed, but inherently homogenous to the composition and nature of the crystal lattice. When the ratio of Ag-Sn: Fe precursor was varied from 1:1 to 1.3:1, particle agglomeration slightly decreased without much difference in their dispersity and homogeneity as can be seen in Fig. 5b. The degree of crystallinity appeared to be accentuated by the use of a mixture of citric acid and glycerol for the wet reduction of Ag-Sn/Fe precursor, as the resulting SFTS

nanoparticles (Fig. 5c) mediated by the mixed capping agent produced heterogeneous microstructures that confirmed the existence of cubic crystal lattice that was found in the powder XRD phase matching. At 250 °C, the degree of crystallinity was seen to have increased, as the nanoparticles produced in citric acid showed a heterogeneous microstructure that is cube-like (Fig. 5d). The increased crystallinity invariably resulted in lesser agglomeration, which portends a competitive growth in the lattice structure of SFTS at the rate when the critical nucleus formed slowly provided a source of attachment for a new one, leading to a longitudinal attachment. A similar result was observed by Roshanghias et al. who synthesised and examined the thermal behaviour of large facet-like particles via agglomeration of ternary Sn-Ag-Cu nanoparticles. The SEM microstructure presented an evident cluster-like nanostructure, with or without a stabilizing agent. Similarly, the mechanochemical synthesis of multinary new and unknown compounds of the type $A_2^{I}B^{II}C^{IV}S_4^{VI}$ and new compounds of the type $A_2^{I}B^{II}C_3^{IV}S_8^{VI}$ gave a cluster in cluster morphology that was confirmed to possess the tetrahedral structure [37].
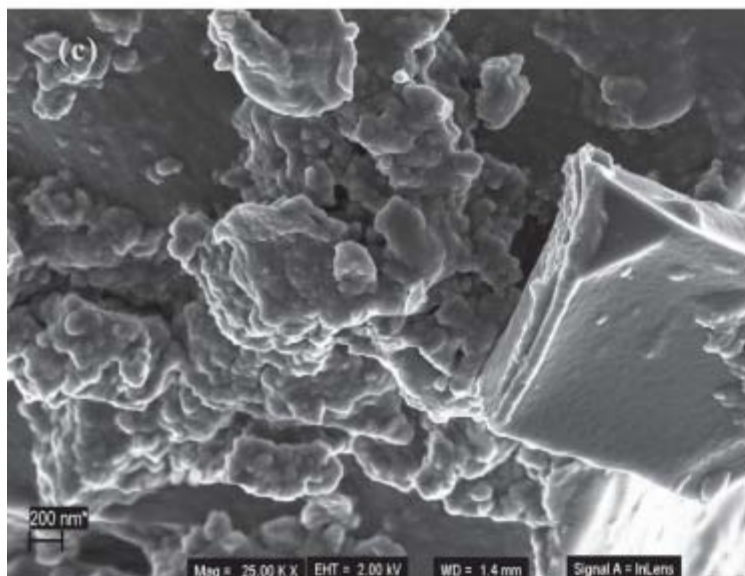
Fig. 5. SEM micrographs of (a) agglomerated SFTS nanocubes in CA with 1:1 mole of Ag-Sn: Fe precursors; (b) CA with 1.3:1 mole of Ag-Sn: Fe precursors; (c) SFTS nanocubes in CA/GLY at 200 °C; (d) SFTS pseudo-nanocubes obtained by heat up in CA at 250 °C.

A representative EDX spectrum of the characterised silver iron tin sulphide nanoparticles in citric acid is presented in Fig. S4 with the characteristic peaks of the compositional elements identified in counts per second, representing the intensity of each atom. The calculated % weight based on the molecular formula mass of $Ag_2FeSnS_4$ is Ag (41.6%); Fe (10.77%); Sn (22.9%); S (24.73%), while the experimental normalized % weight from EDX quantitation is Ag (40.20%); Fe (8.08%); Sn (23.73%); S (22.20%). However, the corresponding atomic % for the formation is Ag (67.39%); Fe (3.86%); Sn (5.49%); S (18.80%). The additional peaks of oxygen, carbon and sodium atoms were due to the capping agents which actively passivated the surface of the nanoparticles to make them reactive. Hence, the establishment of the empirical formula of the unit cell of either the orthorhombic or cubic lattice structure of the canonical $Ag_2FeSnS_4$.

## Optical properties of heterostructure chalcogenide nanoparticles

The UV-Vis spectrophotometry analysis of the $Ag_xFeSnS_y$ nanoparticles gives insight into their optical properties. A dilute solution of each SFTS nanoparticle in acetone was scanned over 250 nm to 1000 nm to determine the absorbance. The optical absorbance spectra were recorded for SFTS NPs in CA at 200 °C, 250 °C, and CA/GLY at 200 °C, as presented in Fig. 6. There is a trend of a gradual decrease in absorbance as wavelength increases, which is typical of the absorbance character of quaternary semiconductors. Tauc's plot was used to estimate $E_g$ by plotting $(\alpha h v)^2$ as a function of the photon energy (eV) and extrapolating the linear region of the spectrum in the band edge region. From the extrapolated Tauc's plot, the bandgap of SFTS NPs synthesised at 200 °C, using citric acid only as the capping agent, gave 1.99 eV. But that of 1.3:1 mole of Ag-Sn: Fe precursor was 1.90 eV. Increasing the reaction temperature to 250 °C, still with citric acid as the capping agent, resulted in a red shift of the bandgap to 1.68 eV. Finally, a mixture of glycerol and citric produced SFTS NPs with a bandgap of 1.58 eV; red-shifted to lower energy. The narrower band edge is crucial to these quaternary chalcogenide photovoltaic and photo-oxidation potentials. Shambharkar & Chowdhury [38] synthesised $Ag_8SnS_6$ using the chemical precipitation method and got a band gap of 1.12 eV, within the required range. All the synthesised quaternary chalcogenides produced have bandgaps within the range of semiconductors (1-3 eV) [39]. It shows that $Ag_xFeSnS_y$ NPs have potential optical applications. We observed a structure-property relationship in these SFTS NPs of the orthorhombic and cubic symmetries. The bandgap for the former is narrower, appears in the range of intermediate light absorbers, and is promising for solar cells.
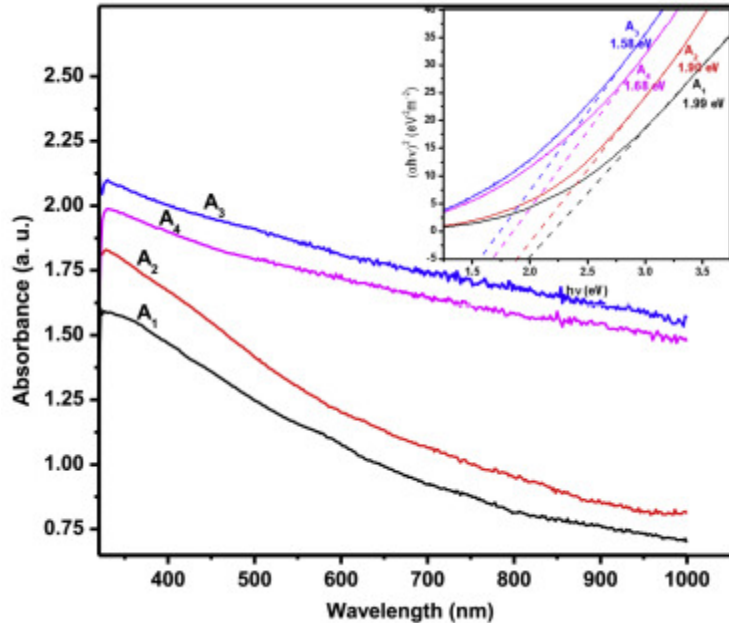
Fig. 6. Optical spectra of $Ag_xFeSnS_y$ NPs in CA at 200 °C, 1:1 mole ratio ($A_1$); 1.3:1 mole ratio ($A_2$); CA/GLY at 200 °C, 1:1 mole ratio ($A_3$) and CA at 250 °C, 1:1 mole ratio ($A_4$) and their respective Tauc's plot, inset ($A_1$ $A_2$ $A_3$ and $A_4$) with extrapolated bandgap energy.

In contrast, the latter cubic structure semiconductors, SFTS NPs in CA/GLY at 200°C and CA at 250°C, exhibited a relatively narrow energy bandgap, 1.58 (Fig. 6 inset $A_3$) and 1.68 eV (Fig. 6 inset $A_4$), respectively making them suitable as light absorbers and potential photocatalysts. Therefore, the structure-property relation can be established and exploited by varying reaction conditions in multijunction semiconductors with intermediate energy bandgap. In a related study by Liu et al. [40], tuning the intermediate-conduction and intermediate-valence band gaps showed that the wurtzite-kesterite structured $Ag_2ZnSnSe_4$ might be a potential light-absorber semiconductor in intermediate-band solar cells. Although the band structures of these materials can be conveniently modified through alloying to boost their ability to harvest visible photons, the choice of precursors and the reaction conditions must be carefully made to optimize their performance.

One of the exciting features of SFTS as transition metal chalcogenides with indirect-direct bandgap is that they show electronic transition traversing from infrared to visible light range. The two-dimensional layer structure of their crystal lattice, where atoms form covalent bonds within the layers, and van der Waal bonds between the layers support their exfoliation or cleavage down to the monolayer (ML) limit. Hence, quaternary materials of SFTS composition could offer promising optical properties in photovoltaic and photocatalytic applications.

# Conclusion

The need to develop potential semiconductors with high optical activity is growing due to the demand for renewable energy and the impact of environmental pollutants that pose an enormous health-associated risk to human and animal lives. The synthesis and study of $Ag_2FeSnS_4$ chalcogenides using eco-friendly coordinating solvents gave rise to single-phase heterostructures showing the presence of the orthorhombic ($Ag_8SnS_6$) and cubic ($AgSnS_2$) crystal systems as the parent phases under varying reaction conditions. The morphological characterisation of these SFTS nanoparticles showed that nanocubes and pseudonanocubes were formed, with different sizes ranging from 22.98 ± 1.67 to 57.26 ± 12.93 nm. The FTIR analysis provided evidence for the surface functionalisation of the SFTS NPs with citric acid and a mixture of citric acid/glycerol. . Further elucidation of the optical property of the HC nanoparticles by Tauc's plot based on the data derived from UV-Vis spectrophotometry measurement revealed that the bandgap ranged from 1.58 to 1.99 eV. At the same time, the UV-Visible spectrophotometry, measured over a range of 250 to 1000 nm, showed broad absorbance between 420 and 800 nm, confirming the optical property of the nanoparticles.

# Funding Statement

# CRediT authorship contribution statement

**Joseph Adeyemi Adekoya:** Conceptualization, Data curation, Formal analysis, Writing – original draft, Supervision. **Michael Onyedikachi Chibuokem:** Investigation, Methodology. **Siphamandla Masikane:** Formal analysis, Writing – review & editing. **Neerish Revaprasadu:** Project administration, Resources.

# Declaration of Competing Interest

The authors declare that no competing interest exists.

# Acknowledgments

# Appendix. Supplementary materials

Download: [Download Word document (2MB)](#)

# References

1. [1]

   P. Balaraman, B. Balasubramanian, W.C. Liu, D. Kaliannan, M. Durai, H. Kamya b, *et al.*
   Sargassum myriocystum-mediated $TiO_2$-nanoparticles and their antimicrobial, larvicidal activities and enhanced photocatalytic degradation of various dyes
   Environ. Res., 204 (2022), Article 112278, 10.1016/j.envres.2021.112278
   View PDFView articleView in ScopusGoogle Scholar

2. [2]

   A. Fouda, S.E.D. Hassan, M.A. Abdel-Rahman, M.M.S. Farag, A. Shehal-deen, A.A. Mohamed, *et al.*
   Catalytic degradation of wastewater from the textile and tannery industries by green synthesized hematite ($\alpha$-$Fe_2O_3$) and magnesium oxide (MgO) nanoparticles
   Curr. Res. Biotechnol., 3 (2021), pp. 29-41, 10.1016/j.crbiot.2021.01.004
   View PDFView articleView in ScopusGoogle Scholar

3. [3]

   J.A. Nasir, Z. ur Rehman, S.N.A. Shah, A. Khan, I.S. Butler, C.R.A. Catlow

   Recent developments and perspectives in CdS-based photocatalysts for water splitting

   J. Mater. Chem. A, 8 (40) (2020), pp. 20752-20780, 10.1039/D0TA05834C
   View in ScopusGoogle Scholar

4. [4]

   X. Bao, Q. She, W. Long, Q. Wu

   Ammonium ultra-selective membranes for wastewater treatment and nutrient enrichment: Interplay of surface charge and hydrophilicity on fouling propensity and ammonium rejection

   Water Res., 190 (2021), Article 116678, 10.1016/j.watres.2020.116678
   View PDFView articleView in ScopusGoogle Scholar

5. [5]

   A. Pakdel Mojdehi, M. Pourafshari Chenar, M. Namvar-Mahboub, M. Eftekhari

Development of PES/polyaniline-modified TiO$_2$ adsorptive membrane for copper removal
Colloids Surf. A Physicochem. Eng. Asp., 583 (2019), Article 123931, 10.1016/j.colsurfa.2019.123931
View PDFView articleView in ScopusGoogle Scholar

6. [6]

Y. Xiong, H. Wan, M. Islam, W. Wang, L. Xie, S. Lü, *et al.*
Hyaluronate macromolecules assist bioreduction (AuIII to Au0) and stabilization of catalytically active gold nanoparticles for azo contaminated wastewater treatment
Environ. Technol. Innov., 24 (2021), Article 102053, 10.1016/j.eti.2021.102053
View PDFView articleView in ScopusGoogle Scholar

7. [7]

A.G. Oliveira, A. JdL, M.C. Montanha, S.M. Lima, LHdC Andrade, A.A. Winkler Hechenleitner, *et al.*
Decontamination and disinfection of wastewater by photocatalysis under UV/visible light using nano-catalysts based on Ca-doped ZnO
J. Environ. Manag., 240 (2019), pp. 485-493, 10.1016/j.jenvman.2019.03.124
View PDFView articleView in ScopusGoogle Scholar

8. [8]

J. Si, J. Gu, H. Luan, X. Yang, L. Shi, Y. Shao, *et al.*
Porous composite architecture bestows Fe based glassy alloy with high and ultra-durable degradation activity in decomposing azo dye
J. Hazard. Mater., 388 (2020), Article 122043, 10.1016/j.jhazmat.2020.122043
View PDFView articleView in ScopusGoogle Scholar

9. [9]

M. Nagamine, M. Osial, K. Jackowska, P. Krysinski, J. Widera-Kalinowska

Tetracycline photocatalytic degradation under CdS treatment

J. Mar. Sci. Eng., 8 (7) (2020), p. 483, 10.3390/jmse8070483
Google Scholar

10. [10]

K.M. Lee, C.W. Lai, K.S. Ngai, J.C. Juan

Recent developments of zinc oxide based photocatalyst in water treatment technology: a review

Water Res., 88 (2016), pp. 428-448, 10.1016/j.watres.2015.09.045
View PDFView articleView in ScopusGoogle Scholar

11. [11]

M. Mishra, D.M. Chun

α-$Fe_2O_3$ as a photocatalytic material: a review
Appl. Catal. A Gen., 498 (2015), pp. 126-141, 10.1016/j.apcata.2015.03.023
View PDFView articleView in ScopusGoogle Scholar

12. [12]

M. Raaja Rajeshwari, S. Kokilavani, S. Sudheer Khan

Recent developments in architecturing the g-$C_3N_4$ based nanostructured photocatalysts: synthesis, modifications and applications in water treatment
Chemosphere, 291 (2022), Article 132735, 10.1016/j.chemosphere.2021.132735
View PDFView articleView in ScopusGoogle Scholar

13. [13]

N. Tahmasebi, Z. Maleki, P. Farahnak

Enhanced photocatalytic activities of $Bi_2WO_6$/BiOCl composite synthesized by one-step hydrothermal method with the assistance of HCl
Mater. Sci. Semicond. Process., 89 (2019), pp. 32-40, 10.1016/j.mssp.2018.08.026
View PDFView articleView in ScopusGoogle Scholar

14. [14]

X. Zhao, Z. Lu, W. Ma, M. Zhang, R. Ji, C. Yi, *et al.*
One-step fabrication of carbon decorated $Co_3O_4$/$BiVO_4$ p-n heterostructure for enhanced visible-light photocatalytic properties
Chem. Phys. Lett., 706 (2018), pp. 440-447, 10.1016/j.cplett.2018.05.056
View PDFView articleView in ScopusGoogle Scholar

15. [15]

D. Cao, Y. Wang, M. Qiao, X. Zhao

Enhanced photoelectrocatalytic degradation of norfloxacin by an $Ag_3PO_4$/$BiVO_4$ electrode with low bias
J. Catal., 360 (2018), pp. 240-249, 10.1016/j.jcat.2018.01.017
View PDFView articleView in ScopusGoogle Scholar

16. [16]

K. Changanaqui, E. Brillas, H. Alarcón, I. Sirés

ZnO/$TiO_2$/$Ag_2Se$ nanostructures as photoelectrocatalysts for the degradation of oxytetracycline in water
Electrochim. Acta, 331 (2020), Article 135194, 10.1016/j.electacta.2019.135194

View PDFView articleView in ScopusGoogle Scholar

17. [17]

W. Du, X. Qian, J. Yin, Q. Gong

Shape- and phase-controlled synthesis of monodisperse, single-crystalline ternary chalcogenide colloids through a convenient solution synthesis strategy

Chem. Eur. J., 13 (31) (2007), pp. 8840-8846, 10.1002/chem.200700618
View in ScopusGoogle Scholar

18. [18]

G. Delgado, P. Gallardo, J. Aitken, A. Cárdenas, I. Brito

The new P-chalcopyrite compound $Cu_2FeIn_2Se_5$; synthesis, thermal analysis (DTA), and crystal structure analysis by X-ray powder diffraction (XRPD)
Rev. Mex. Fís., 67 (2021), p. 18, 10.31349/revmexfis.67.18
View in ScopusGoogle Scholar

19. [19]

P. Grima-Gallardo, S. Torres, M. Quintero, L. Nieves, E. Moreno, GE. Delgado

Phase diagram of $(CuInSe_2)_{1-x}(FeSe)_x$ alloys
J. Alloy. Compd., 630 (2015), pp. 146-150, 10.1016/j.jallcom.2015.01.015
View PDFView articleView in ScopusGoogle Scholar

20. [20]

G.E. Delgado, A.J. Mora, P. Grima-Gallardo, S. Durán, M. Muñoz, M. Quintero

Preparation and crystal structure characterization of $CuNiGaSe_3$ and $CuNiInSe_3$ quaternary compounds
Bull. Mater. Sci., 33 (5) (2010), pp. 637-640, 10.1007/s12034010-0097-6
View in ScopusGoogle Scholar

21. [21]

K.W. Cheng, W.T. Tsai, Y.H. Wu

Photo-enhanced salt-water splitting using orthorhombic $Ag_8SnS_6$ photoelectrodes in photoelectrochemical cells
J. Power Sources, 317 (2016), pp. 81-92, 10.1016/j.jpowsour.2016.03.086
View PDFView articleView in ScopusGoogle Scholar

22. [22]

K.Y. Lee, K.W. Cheng

Chemical synthesis of orthorhombic $Ag_8SnS_6$/zinc oxide nanorods photoanodes for photoelectrochemical salt-water splitting
J. Mater. Sci. Mater. Electron., 32 (8) (2021), pp. 10532-10548, 10.1007/s10854-021-05709-9
View in ScopusGoogle Scholar

23. [23]

T. Ghrib, A.L. Al-Otaibi, M.A. Almessiere, I.B. Assaker, R. Chtourou

High thermoelectric figure of merit of $Ag_8SnS_6$ component prepared by electrodeposition technique
Chin. Phys. Lett., 32 (12) (2015),
Article 127402, 10.1088/0256307X/32/12/127402
View in ScopusGoogle Scholar

24. [24]

W.Q. Hu, Y.F. Shi, L.M. Wu

Synthesis and shape control of Ag8SnS6 submicropyramids with high surface energy

Cryst. Growth Des., 12 (7) (2012), pp. 3458-3464, 10.1021/cg201649d
View in ScopusGoogle Scholar

25. [25]

P.R. Selvakannan, S. Mandal, S. Phadtare, R. Pasricha, M. Sastry

Capping of gold nanoparticles by the amino acid lysine renders them water-dispersible

Langmuir, 19 (8) (2003), p. 35459, 10.1021/la026906v
Google Scholar

26. [26]

D.P. Stankus, S.E. Lohse, J.E. Hutchison, JA. Nason

Interactions between natural organic matter and gold nanoparticles stabilized with different organic capping agents

Environ. Sci. Technol., 45 (8) (2011), pp. 3238-3244, 10.1021/es102603p
View in ScopusGoogle Scholar

27. [27]

X. Wang, J. Stöver, V. Zielasek, L. Altmann, K. Thiel, K. Al-Shamery, *et al.*
Colloidal synthesis and structural control of PtSn bimetalliC nanoparticles
Langmuir, 27 (17) (2011), Article 1105261, 10.1021/la201829y

Google Scholar

28. [28]

N. Al-Salim, A. Young, R. Tilley, A. McQuillan, J. Xia

Synthesis of CdSeS nanocrystals in coordinating and noncoordinating solvents: solvent's role in evolution of the optical and structural properties

Chem. Mater., 19 (2007), 10.1021/cm070818k
Google Scholar

29. [29]

M.D. Khan, N. Revaprasadu

Metal–organic precursors for ternary and quaternary metal chalcogenide nanoparticles and thin films

Nanoscience, 6 (2020), pp. 1-31, 10.1039/9781788017053-00001
Volume
Google Scholar

30. [30]

J.A. Adekoya, M.D. Khan, N. Revaprasadu

Phase transition in $Cu_{2+x}SnS_{3+y}$ ($0 \leq x \leq 2$; $0 \leq y \leq 1$) ternary systems synthesized from complexes of coumarin derived thiocarbamate motifs: optical and morphological properties
RSC Adv., 9 (61) (2019), pp. 35706-35716, 10.1039/C9RA07376K
View in ScopusGoogle Scholar

31. [31]

W. Hoisang, T. Uematsu, T. Torimoto, S. Kuwabata

Surface ligand chemistry on quaternary $Ag(In_xGa_{1-x})S_2$ semiconductor quantum dots for improving photoluminescence properties
Nanoscale Adv., 4 (3) (2022), pp. 849-857, 10.1039/D1NA00684C
View articleView in ScopusGoogle Scholar

32. [32]

R.A. Ismail, R.G. Kadhim, A. WaM

Effect of multiwalled carbon nanotubes incorporation on the performance of porous silicon photodetector

Optik, 127 (19) (2016), pp. 8144-8152, 10.1016/j.ijleo.2016.06.018
View PDFView articleView in ScopusGoogle Scholar

33. [33]

S.O. Ajayi, C.O. Ehi-Eromosele, A. KO

Energy and fuels: sol-gel synthesized core shell
$0.5Li_2MnO_3 \cdot 0.5LiNi0.5Mn_{0.3}Co_{0.2}O_2$ material: effect of mixed fuel (Citric
Acid and Ammonium Acetate) on the structural properties
Ayeni AO, Sanni SE, Oranusi SU, editors
Bioenergy and Biochemical Processing Technologies: Recent Advances and
Future Demands, Springer International Publishing, Cham (2022), pp. 45-
50, 10.1007/978 3-030-96721-5_5
View in ScopusGoogle Scholar

34. [34]

C.O. Ehi-
Eromosele, B.I. Ita, E.E.J. Iweala, K.O. Ogunniran, J.A. Adekoya, F.E. Ehi-
Eromosele

Structural and magnetic characterization of $La_{0.7}Sr_{0.3}MnO_3$ nanoparticles
obtained by the citrate-gel combustion method: Effect of fuel to oxidizer
ratio
Ceram. Int., 42 (1) (2016), pp. 636-643, 10.1016/j.ceramint.2015.08.158
Part A
View PDFView articleView in ScopusGoogle Scholar

35. [35]

P. Kush, S. Deka

Photoelectrical properties of surfactant-free kesterite
$Cu_2ZnSnSe_4$ hydrophilic nanocrystal ink and the stability in polar
solvents
J. Nanoparticle Res., 16 (9) (2014), p. 2600, 10.1007/s11051-014-2600-2
View in ScopusGoogle Scholar

36. [36]

H.G. Manyar, P. Iliade, L. Bertinetti, S. Coluccia, G. Berlier

Structural and spectroscopic investigation of ZnS nanoparticles grown in
quaternary reverse micelles

J. Colloid Interface Sci., 354 (2) (2011), pp. 511-516, 10.1016/j.jcis.2010.11.033
View PDFView articleView in ScopusGoogle Scholar

37. [37]

E.M. Heppke, T. Bredow, M. Lerch

Mechanochemical synthesis and crystal structure evaluation of Na$_2$ZnSnS$_4$

Z. Anorg. Allg. Chem. (2022), p. e202200216, 10.1002/zaac.202200216

View in ScopusGoogle Scholar

38. [38]

B.H. Shambharkar, A.P. Chowdhury

Ethylene glycol mediated synthesis of Ag8SnS6 nanoparticles and their exploitation in the degradation of eosin yellow and brilliant green

RSC Adv., 6 (13) (2016), pp. 10513-10519, 10.1039/C5RA25051J

View in ScopusGoogle Scholar

39. [39]

N. Gaponik, D.V. Talapin, A.L. Rogach, K. Hoppe, E.V. Shevchenko, A. Kornowski, *et al.*

Thiol capping of CdTe nanocrystals: an alternative to organometallic synthetic routes

J. Phys. Chem. B., 106 (29) (2002), pp. 7177-7185, 10.1021/jp025541k

View in ScopusGoogle Scholar

40. [40]

Q. Liu, Z. Cai, D. Han, S. Chen

Natural intermediate band in I$_2$-II-IV-VI$_4$ quaternary chalcogenide semiconductors

Sci. Rep., 8 (1) (2018), p. 1604, 10.1038/s41598-018 19935-5

View in ScopusGoogle Scholar

# Cited by (2)

- Anionic framework descriptors and microstructure affects on optical parameters of Ag$_{7+x}$(P$_{1-x}$Ge$_x$)S$_6$ single crystals
  2023, Optical Materials

  Show abstract

- Chalcogenides and their nanocomposites in photocatalytic reactions
  2023, Metal-Chalcogenide Nanocomposites: Fundamentals, Properties and Industrial Applications

  Show abstract

# Recommended articles

- Long-term spatio-temporal variability and change in rainfall over Ghana (1960–2015)
  Scientific African, Volume 19, 2023, Article e01588
  Steve Ampofo, …, Leonard K. Amekudzi
  View PDF
- Assessment of reservoir performance under climate change: A case study in Shumbrite reservoir, South Gojjam sub-basin, Ethiopia
  Scientific African, Volume 19, 2023, Article e01484
  Tadege A. Worku, …, Mekash S. Kifelew
  View PDF
- A systematic study of the effect of graphene oxide and reduced graphene oxide on the thermal degradation behavior of acrylonitrile-butadiene rubber in air and nitrogen media
  Scientific African, Volume 19, 2023, Article e01501
  Bismark Mensah, …, Samuel Kwofie
  View PDF
  Show 3 more articles

# Article Metrics

Citations

- Citation Indexes:2

Captures

- Readers:9

Mentions

- News Mentions:1

Social Media

- Shares, Likes & Comments:50



View details


- About ScienceDirect
- Remote access
- Shopping cart
- Advertise

- Contact and support
- Terms and conditions
- Privacy policy